(This is a sample cover image for this issue. The actual cover is not yet available at this time.)

Spectral difference analysis and airborne imaging classification for citrus greening infected trees

Xiuhua Li [a,b], Won Suk Lee [b,*], Minzan Li [a], Reza Ehsani [c], Ashish Ratn Mishra [c], Chenghai Yang [d], Robert L. Mangan [d]

[a] Key Laboratory of Modern Precision Agriculture Integration Research, MOE, China Agricultural University, Beijing 100083, China
[b] Department of Agricultural & Biological Engineering, University of Florida, Gainesville, FL 32611, United States
[c] Citrus Research and Education Center, University of Florida, 700 Experiment Station Road, Lake Alfred, FL 33850, United States
[d] USDA-ARS, Kika de la Garza Subtropical Agricultural Research Center, Weslaco, TX 78596, United States

ARTICLE INFO

ABSTRACT

Citrus greening, also called Huanglongbing (HLB), became a devastating disease spread through citrus groves in Florida, since it was first found in 2005. Multispectral (MS) and hyperspectral (HS) airborne images of citrus groves in Florida were acquired to detect citrus greening infected trees in 2007 and 2010. Ground truthing including field and indoor spectral measurement, infection status along with GPS coordinates was conducted for both healthy and infected trees. Ground spectral measurements showed that healthy canopy had higher reflectance in the visible range, and lower reflectance in the near-infrared (NIR) range than HLB infected canopy. Red edge position (REP) also showed notable difference between healthy and HLB canopy. But the difference in the NIR range and REP were comparably more sensitive to the environment or the background noise. Accuracy for separating HLB and healthy samples reached more than 90% when a simple REP threshold method was implemented in the ground reflectance datasets, regardless of field or indoor measurement; but it did not work well with the HS images because of its low spatial resolution. Support vector machine (SVM) was able to provide a fast, easy and adoptable way to build a mask for tree canopy. High positioning error of the ground truth in the 2007 HS image led to validation accuracy of less than 50% for most of classification methods. In the 2010 image from Southern Gardens (SG) grove, with better ground truth records, higher classification accuracies (about 90% in training sets, more than 60% in validation sets for most of the methods) were achieved. Disease density maps were also generated from the classification results of each method; most of them were able to identify the severely infected areas. Simpler classification methods such as minimum distance (MinDist) and Mahalanobis distance (MahaDist) showed more stable and balanced detection accuracy between the training and validation sets in the 2010 images. Their similar infection trend with ground scouted maps showed a promising future to manage HLB disease with airborne spectral imaging.

© 2012 Elsevier B.V. All rights reserved.

1. Introduction

1.1. Citrus Industry and HLB

As a major fruit crop in Florida, citrus produced about $1.47 billion in 2009–2010, compared to $2.88 billion throughout the US, according to the citrus statistics by National Agricultural Statistics Services (USDA, 2010). The whole citrus industry has about $9 billion economic impact in Florida where nearly 569,000 acres of citrus groves exist.

However, this citrus industry is now greatly threatened by the citrus greening disease (also known as Huanglongbing or HLB in

short). By February 2010, more than 3000 sections (one section is one square mile) were found infected by this disease in 34 counties as shown in Fig. 1a (DPI, 2010). HLB infected trees have the initial appearance of asymmetric yellow patches on some of its leaves (Fig. 1b). As the bacteria spread within the tree, the entire canopy progressively turns yellowish which may superficially resemble zinc deficiency. Fruit from severely infected trees are small, bitter, and often irregular in shape, which will totally destroy their economic value. The vector *Diaphorina citri Kuwayama* which originated from Asia was discovered in June 1998 in Florida (Halbert and Manjunath, 2004), and the disease itself was first found in August 2005 in south Miami-Dade County, Florida (Manjunath et al., 2008).

The definitive diagnosis methods are mainly based on genetic methodology such as polymerase chain reaction (PCR) (Jagoueix
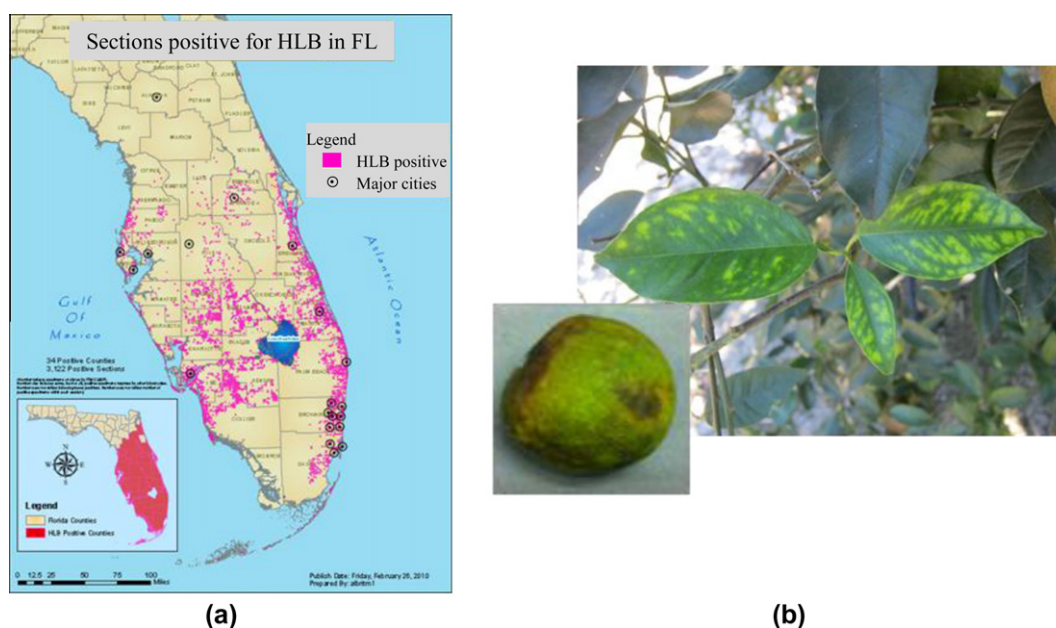
Fig. 1. HLB infected sections and disease symptom: (a) HLB infected sections (marked in red) in Florida (DPI, 2010), and (b) HLB symptom on leaves and fruit. (For interpretation of the references to color in this figure legend, the reader is referred to the web version of this article.)

et al., 1996). No effective and environmentally sound cure method has been found yet. The only preventative measure implemented till now to slow down or reduce further infection is to remove the infected trees.

1.2. Citrus greening detection technologies

Although PCR test is so far the most accurate method to confirm HLB, samples should be first collected by trained workers, and then tested individually in a laboratory. The sampling and analysis process turns out to be highly labor intensive and time consuming, especially considering the wide grove area and the large number of trees. So it is urgently required to find some other ways to quickly and accurately detect the infected trees.

Spectral reflectance (commonly measured in the visible and near-infrared (NIR) spectral range) differs when the chemical components in the surface or subsurface of crop canopy change. This causality provided researchers a nondestructive way to sense the change happening inside the object. In agriculture, many studies related to spectral features have been conducted to predict crop leaf chlorophyll content, nitrogen content, canopy diseases, etc. Pydipati (2004) and Qin et al. (2009) used color camera and hyperspectral imaging system to differentiate some common symptomatic citrus diseases by taking pictures of citrus' leaves and fruit under laboratory environment. Since one of the most obvious symptoms of HLB is the change of canopy color to lighter green and yellow, this imaging method could also be applied to detect HLB disease. Gonzalez-Mora et al. (2010) set up a ground based prototype of hyperspectral sensing system which was designed to identify HLB infected trees, but the experimental result was much affected by unrealistic illumination condition and unfavorable timing. Fourier transform infrared–attenuated total reflection (FT-IR–ATR) spectroscopy was used by Hawkins et al. (2010) to test the HLB disease in its earlier pre-symptomatic stages. As a substitute method of a PCR test, it took only minutes rather than hours to test a sample, and had a very high accuracy of 95%. However, for this method, leaf samples needed to be collected, dried, and ground before analyzed.

Although the methods based on machine vision and spectrora-diometer mentioned above had a promising accuracy to distinguish

the diseased fruit or trees from healthy ones, it is still time consuming when applied to a large citrus grove due to their ground based detection. Another extreme choice is satellite imagery which has a large field of view and has also been widely used in agricultural applications, such as vineyard leaf area estimation (Johnson et al., 2003), sugarcane harvest detection (Hajj et al., 2009), etc. But it is difficult to conduct tree-based disease detection due to its coarse spatial resolution. This problem can be solved by adopting airborne imaging which has a good balance of area coverage and image resolution compared to either ground measurement or satellite imagery.

Many studies on hyperspectral (HS) and multispectral (MS) image processing have been conducted in recent years, since satellite and aircraft remote images are becoming easier to acquire. Noise reduction is one of the most important preprocessing steps, especially for HS image which has large amount of correlated redundancy among its hundreds of different wavelength bands. Approaches such as principle component analysis (PCA), minimum noise fraction (MNF), artificial neural network (ANN), etc. could be used for noise reduction or bands selection (Bajwa et al., 2004; Boardman and Kruse, 1994; Green et al., 1988).

Kumar et al. (2010) investigated several endmember detection algorithms to distinguish HLB infected citrus trees from healthy ones based on MS and HS images, but more sufficient and convincing ground spectral analysis is needed, and the classification accuracy needs to be further improved. Huang et al. (2007) derived photochemical reflectance index (PRI) from both in-situ spectral reflectance measurement and airborne HS image to evaluate the yellow rust infection status in wheat, and the coefficients of determination between PRI and infection severity reached to 0.97 and 0.91 using in-situ spectral reflectance and airborne HS image, respectively.

Artificial neural network and support vector machines (SVMs) are also used in image pixel classification. In order to find out which method is more suitable for land use classification, Candade and Dixon (2004) compared the application result with remote-sensing image classification by using these pattern recognition techniques.

In a study conducted by Plaza et al. (2009), good classification performance was demonstrated by SVMs using spectral signatures

as input features, and was further improved by taking advantage of semi-supervised learning and contextual information. Several classification algorithms for pattern recognition had also been tested in the mapping of tropical forest cover using airborne HS data in a research conducted by Shafri et al. (2007). Results of maximum likelihood, spectral angle mapping (SAM), artificial neural network (ANN), and decision tree classifiers were compared and evaluated.

Vegetation indices are also widely used for crop status evaluation or classification. Shafri and Hamdan (2009) used vegetation indices and red edge techniques derived from airborne hyperspectral image to detect ganoderma basal stem rot disease in oil palm plantations, and reported that red edge based techniques reached the highest accuracy of more than 80%. Qin and Zhang (2005) used ratio indices and stand difference indices from the four-band multispectral airborne image to detect rice sheath blight disease, and reached a highest correlation coefficient of 0.68 with field disease index. Tian et al. (2011) improved a technique to calculate red edge position (REP) for leaf nitrogen concentration (LNC) prediction in rice, and compared the accuracy with other techniques such as linear extrapolation, Lagrangian technique, etc. by applying to a Hyperion image, and reached higher coefficient of determination with leaf area index and leaf nitrogen concentration than other techniques.

Although so many studies about remote sensing technologies have been conducted, its application on HLB detection in citrus groves was just started. In this study, advantages of both ground and airborne remote sensing were utilized to find the spectral differences between HLB and healthy citrus canopies. Several classification and spectral mapping methods were later implemented in airborne MS and HS images. Their performances and adaptability to detect HLB infected canopy in citrus groves were then compared and evaluated.

2. Materials and methods

2.1. Image acquisition in 2007 and 2010

Airborne MS and HS images were acquired in 2007 and 2010, at a commercial citrus grove named Southern Garden (SG) in Hendry County, FL, and a research grove in the Citrus Research and Education Center (CREC, affiliated to the University of Florida), Lake Alfred, FL.

The 2007 HS image was taken at northern part of the SG grove on November 3rd. The region of interest (ROI) spread across more than 730 ha. The center coordinates were 26.385523°N, 80.956000°W. Two orange varieties, *Valencia* and *Hamlin*, were grown in this area. An AISA Eagle sensor was configured to collect the HS data with 128 bands (ranging from 397 to 995 nm with an interval of 4.7 nm). The raw data were radiometrically calibrated to radiance and then atmospherically corrected to reflectance by the FLAASH module in ENVI software (version 4.6, ITT VSI, White Plains, NY, USA). The final reflectance percentage values were multiplied a factor of 100. The calibrated data were then georeferenced using corresponding GPS and inertial measurement unit (IMU) information. The final mosaic image which was presented in UTM N17 projection with the datum of WGS-84 had a spatial resolution of 0.7 m, and the estimated accuracy was approximately 1–2 pixels.

On December 3rd in 2010, MS and HS images were taken upon both the SG and CREC groves. Two orange blocks (with a variety of *Valencia*) at the southwest corner (center coordinates of 26.318096°N and 80.957778°W) was chosen as a study area in the SG grove; and one block (center coordinates of 28.104920°N and 81.714020°W) was chosen in the CREC grove. Two prototype MS and HS imaging systems (shown in Fig. 2a) developed by Yang
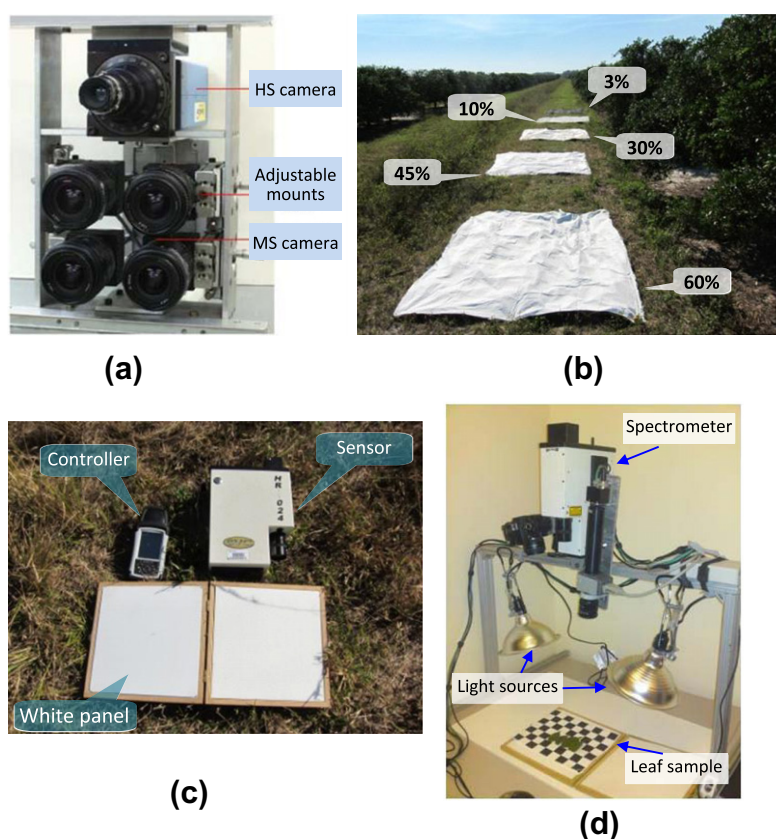

Fig. 2. 2010 experiment site and equipment: (a) HS and MS imaging systems (Yang, 2010), (b) citrus grove with calibration tarps of different gray levels indicated, (c) HR-1024 handheld spectrometer along with a white panel, and (d) indoor platform for spectral measurement.

et al. (2003) and Yang (2010) were used in this experiment. The MS system consisted of four high resolution CCD cameras with four band-pass filters at the wavebands of blue (430–470 nm), green (530–570 nm), red (630–670 nm), and NIR (810–850 nm). The HS imaging system integrated a CCD camera and an imaging spectrograph which dispersed radiation into 128 bands in the range of 457.2–921.7 nm (with an interval of 3.6 nm), and scanned in the along-track direction. Alignment for the MS images and geometric correction for the HS images were conducted. For atmospheric calibration, five 3 m × 3 m tarps with different gray levels (3%, 10%, 30%, 45%, and 60%) were placed at an open area next to the citrus blocks while taking images, as shown in Fig. 2b. Their ground reflectance was also measured in both groves with a handheld spectrometer (HR-1024, Spectra Vista Corporation, Poughkeepsie, NY, USA, more detailed information found in Section 2.2) (Fig. 2c). By matching the ground reflectance of those tarps with their ROIs from images, empirical line was developed to radiometrically calibrate the raw digital number (DN) to reflectance. With corner coordinates collected with an RTK GPS equipment (HiPer XT, Topcon, Livermore, CA, USA), all the MS and HS images were georeferenced to UTM N17 projection with the datum of WGS-84. The MS images were resampled with 0.5 m resolution, and the HS images were resampled with 1 m resolution. Basic information of these five images is listed in Table 1.

2.2. Ground truth measurement

In the 2007 experiment, the whole ROI was scouted by the grove workers to check the infection status of each tree; however no PCR tests were performed to confirm the HLB infection. A total of 7972 HLB infected trees along with their GPS coordinates were recorded, however the positioning error was about 1–3 m. No ground spectral reflectance was measured. The 2007 experiment was only used as a counterexample to prove the importance of the ground truthing. In the 2010 experiment, four classes of

infection status were established based on symptom visibility and PCR results at the SG grove; another five classes only based on tree infection severity were established at the CREC grove. Table 2 lists the detailed information for all the classes.

Three types of ground truthing were investigated:

(a) Field and indoor spectral reflectance measurement for all the classes.
(b) PCR tests to confirm HLB infected status of leaf samples.
(c) Coordinates recording for all the measured trees by using an RTK GPS receiver (HiPer XT, Topcon, Livermore, CA, USA) with a static horizontal accuracy of 3 mm.

Both field and indoor reflectance at the SG grove were measured by the handheld spectrometer which was also used in the tarp measurement. It has a spectral range of 348–2505 nm with an interval of 3 nm. A white reference panel made from polytetrafluoroethylene (PTFE) material was used for calibration. The field measurement took advantage of solar radiation, and the indoor measurement adopted an artificial light source.

The field measurement at the CREC grove was also carried out with the same handheld spectrometer, but indoor measurement for leaf samples, as well as branch and fruit samples was conducted with another UV–VIS–NIR spectrophotometer (Cary 500 Scan, Varian, Palo Alto, CA, USA), which had better spectral resolution and an integrating sphere for reflectance measurement. The spectral range was 200–2500 nm with a 1 nm interval.

2.3. Spectral feature analysis

Spectral features derived from original reflectance, such as absorption and reflectance characteristics, first derivative (1D), red edge position, etc. from both ground measurement and airborne images were analyzed and discussed.

2.3.1. Spectral feature analysis from ground measurement

Mean spectra and 1D of every canopy class from the 2010 indoor measurements in the CREC grove were calculated and are shown in Fig. 3. In the main plots, the dashed and dotted lines represent classes with different HLB infection severity. The green and red solid lines represent the mean spectra for all the healthy and HLB infected samples, respectively. Those numbers in the parentheses are the sample numbers for each class. The upper right subplot shows the 1D signature which was pre-processed with 11-step moving average for each class.

The indoor spectra shown in Fig. 3 were all about leaf samples instead of canopy. The spectrophotometer used in the indoor experiment had its own light source, and every leaf sample was placed in an enclosed chamber, thus the result was very precise and reliable. In Fig. 3, samples with different infection severity

Table 1
Basic information for images used to detect HLB diseased canopy.

Images	Spectral bands	Spatial resolution (m)
2007 SG_HS	128-band HS image from 397 to 995 nm (4.7 nm interval)	0.7
2010 SG_HS 2010 CREC_HS	128-band HS image from 457.2 to 921.7 nm (3.6 nm interval), acquired at the Southern Gardens grove and CREC, respectively	1.0
2010 SG_MS 2010 CREC_MS	4-band MS image (at 450, 550, 650, and 830 nm), acquired at the Southern Gardens grove and CREC, respectively	0.5

Table 2
Brief description of four classes of leaf samples: only the class marked with '*' was used to build a healthy library, and the class marked with '**' was used to build a HLB library. The other classes were not used in any library development. In the SG grove, "HEA" stands for "healthy", "S" stands for "symptom", "NS" stands for "non-symptom", "P" stands for "positive", and "N" stands for "negative".

| Imaging location	Classes	Tree infection status	Infection status of sampled leaves
SG grove	HEA_PCR_N*	Healthy	No HLB symptom, PCR tested negative
	S_PCR_P**	HLB infected	With HLB symptom, PCR tested positive
	NS_PCR_N	HLB infected	No HLB symptom and PCR tested negative
	NS_PCR_P	HLB infected	No HLB symptom but PCR tested positive
CREC grove	HEALTHY	Healthy	No HLB symptom and PCR tested negative
	HLB_L	HLB infected	Low HLB infection, PCR tested positive
	HLB_M	HLB infected	Medium HLB infection, PCR tested positive
	HLB_H	HLB infected	High HLB infection, PCR tested positive
	HLB_S	HLB infected	Severe HLB infection, PCR tested positive
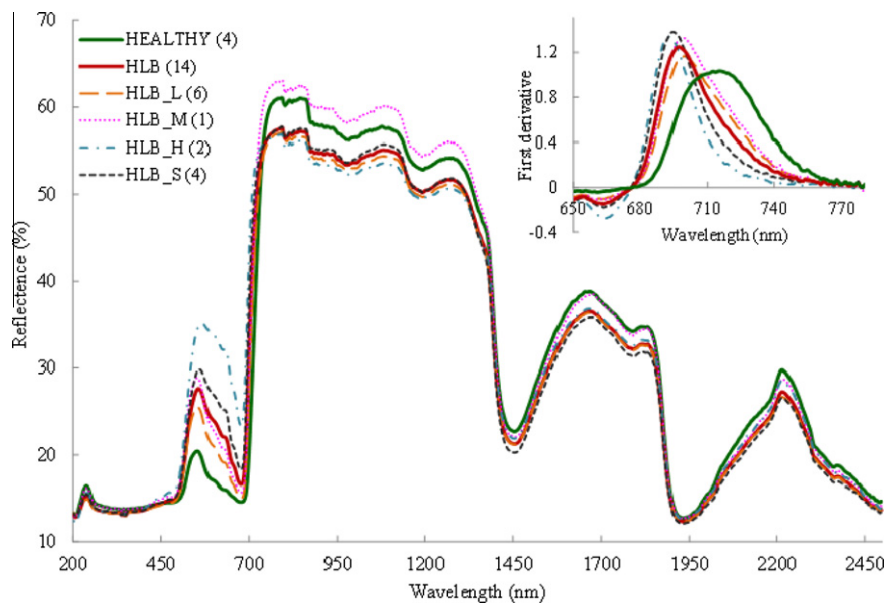
Fig. 3. Mean spectra and first derivatives of 2010 indoor measurement of the samples obtained from the CREC grove.

mainly show different levels of reflectance. Roughly, the more severe the infection was, the higher reflectance the sample had in the visible range (400–700 nm). But in the NIR range (700–2500 nm), most of the infected samples had lower reflectance than healthy ones, except HLB_M.

The difference in the visible range was commonly found in other research; it was mainly caused by the decrease of chlorophylls with the presence of the HLB disease. It was also found that the diseased leaves had certain damage or change on the inner cellular structure which, in most of the cases, led to lower reflectance in the NIR range (Knipling, 1970).

From the 1D plot, obvious difference between healthy and HLB reflectance is presented. The infected leaves, regardless of their severity difference, have similar peak positions in the red edge spectral range (this peak is commonly defined as red edge position or REP by Horler et al., 1983), which are far from that of the healthy

leaves. This characteristic provided a promising way to discriminate HLB from healthy samples.

The only exception is HLB_M which shows different relationship with healthy samples in the NIR range. But since this class included just one sample, the causality is difficult to analyze. It might be attributed to other kind of inner structure change which was caused by other disease or nutrient deficiency; or it might be considered as an evidence to show that the HLB disease could cause variable changes to the inner structure, especially combining with the field measurement results.

The field spectral measurement results at the CREC and SG groves are shown in Figs. 4 and 5, respectively. A passive spectrometer other than the active spectrophotometer was used in the field measurement, and the reflectance spectra were calibrated with a white panel. However, notable error could be introduced if the calibration frequency did not catch the radiation change, or the angle
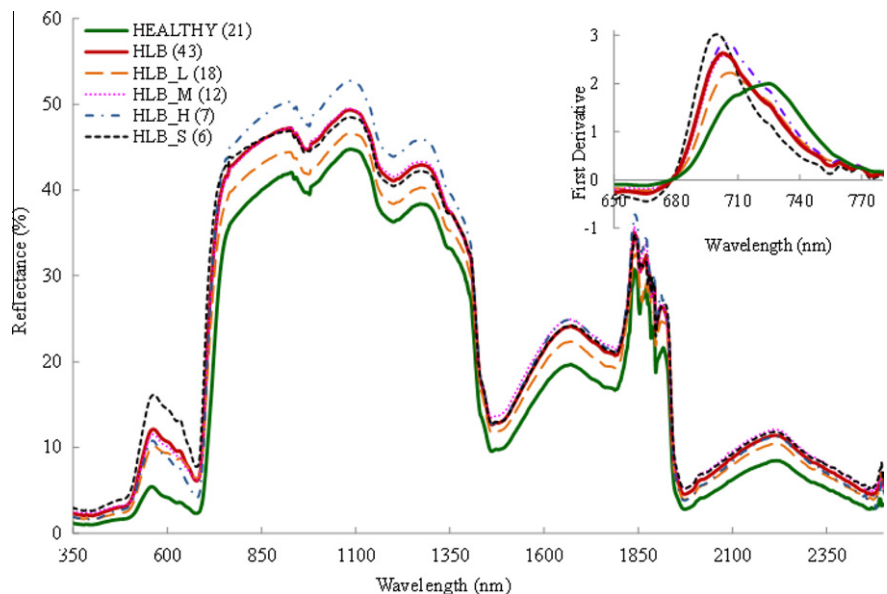

Fig. 4. Mean spectra and first derivatives of 2010 field measurement at the CREC grove.
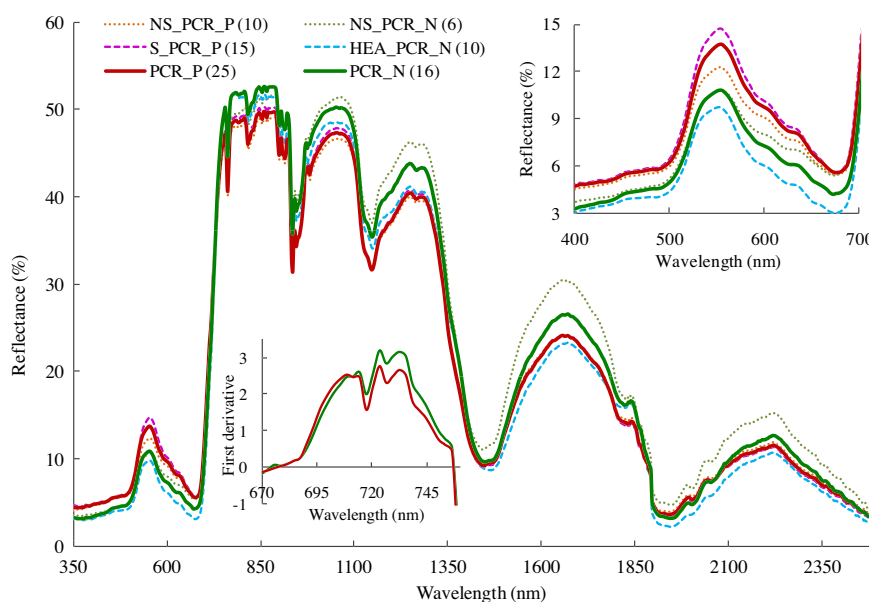
Fig. 5. Mean spectra and first derivatives of 2010 field measurement at the SG grove.

between solar incident light and object surface varied a lot. One more important difference from spectrophotometer measurement was that even the spectrometer had a field of view (FOV) of only 4°, the targeting area still contained other background information and radiation scattered from nearby objects. In the CREC experiment, calibration was conducted before every canopy measurement, and the white panel was kept at the same direction as targeted leaf surface. But in the SG experiment, calibration was only conducted once in a while.

In the CREC field result, the relationships between HLB and healthy canopies in the visible and REP range are almost consistent with the CREC indoor result, but quite different in the NIR range. In the SG field result, the REP difference was not as clear as in other experiments, showing that this indicator was also sensitive to background. The different relationship in the NIR range, on one hand, supported the conclusion that HLB disease can cause variable changes in the NIR range; on the other hand, it also implied that the background had a qualitative influence on the reflectance in the NIR range.

Since the samples were categorized by the symptom visibility and PCR result in the SG experiment, the NS_PCR_P was considered as being in the early stage of HLB disease because no visible symptom had been developed yet. Then another interesting point could be noticed in Fig. 5 that even though NS_PCR_P did not have any visible symptom, it still showed similar spectral reflectance with symptomatic samples (S_PCR_P), suggesting a possibility to detect the disease at early stage.

2.3.2. Spectral feature analysis from MS and HS images

ENVI (version 4.8, ITT VSI, White Plains, NY, USA) was used for the MS and HS image analysis. First, pixels for different classes and land covers were collected to compare their spectral difference. In the 2007 hyperspectral image, due to the notable ground truth positioning error, only infected trees rather than specific infected canopies could possibly be determined. In this case, four neighbor pixels from the center of each infected tree were collected to build an HLB infected library. Five other libraries for healthy tree canopy, grass, sand (bare ground in white color), soil (bare ground in sienna color), and shadow were also manually collected from this image. Trees which were not marked in the ground truthing were considered as healthy ones, and were randomly picked to build a healthy

canopy library. Grass was found between rows and at the edge of every block, and large area of shadow was formed at the east side of every tree since the image was taken around 4 PM.

Mean spectra for those six libraries are plotted in Fig. 6. Numbers in the parentheses in the legend area indicate the number of pixels used for the mean calculation. This plot shows that sand, soil, shadow, and grass have obvious spectral difference than tree canopies, but HLB infected and healthy canopies have much less difference between them. The mean reflectance of HLB pixels is slightly higher than that of healthy ones in both the visible and NIR range. This trend is the same as the results of the 2010 CREC field measurement.

In the 2010 images, more accurate ground truthing was implemented. However, the hyperspectral image from the CREC grove was severely distorted that it was not suitable for classification, so only images from the SG grove were used for further analysis. The HS image from the SG grove, though, which was acquired by a pushbroom HS imaging prototype, still had an along-track distortion due to the decreasing flight speed. As a result, the later part of the original HS image had slightly higher spatial resolution than the previous one. After being georeferenced with corner
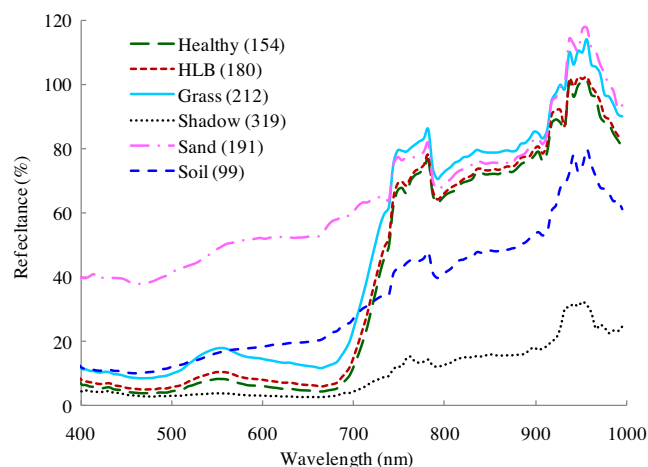

Fig. 6. Mean spectra of each class in the 2007 HS image.

coordinates, the later part accumulated an offset of up to 6 pixels in the opposite flight direction. After comparing with the MS images, the ground truth vectors for the HS image were adjusted so that the positioning error decreased to approximately 1–2 pixels. HLB library was built from S_PCR_P class, and healthy library was built from HEA_PCR_N class. Four adjacent pixels were collected at each location in the MS image, but only 1 pixel was picked in the HS image due to its lower spatial resolution. Several outliers were excluded from spectral libraries after exporting all the data to n-D visualizer. The mean spectra from the HLB and healthy libraries are shown in Fig. 7. HLB shows higher reflectance than healthy canopy from the visible range through the NIR range in both images, consistent with that of the 2007 image.

2.3.3. REP analysis

As found earlier in this study from the first derivatives (1Ds) of healthy and HLB spectra, difference of REP between those two classes was more distinguishable and less sensitive to the environment than that of original reflectance. Thus, a further analysis utilizing REP technology was conducted to evaluate its applicability for classification. The REP difference in the 2010 CREC ground measurement was obviously noticed in Figs. 3 and 4, but hard to distinguish in the 2010 SG field measurement, since it had several peaks in that range. So this time, the dataset from the 2010 SG ground measurement was used to quantize the difference at REP range.

When the first derivative curve is continuous and with only one peak near the red edge, REP can be easily determined by solving an equation of the second derivative being equaled to zero, i.e., finding the inflection point. But in the case of double or more peaks appearing in 1D curve, like the one shown in 1D subplot in Fig. 5, which commonly exists (Boochs et al., 1990; Cho and Skidmore, 2006; Smith et al., 2004), this method does not work properly. In this study, two interpolation techniques termed three-point Lagrangian interpolation (Dawson and Curran, 1998) and four-point linear extrapolation (Cho and Skidmore, 2006) were used to calculate REP from both the ground measurement and HS images.

In the 2010 SG ground experiments, 45 and 260 samples in total were measured in field and indoor experiment, respectively. First derivatives at 688.5, 706.5, and 736.5 nm were chosen for REP calculation with three-point Lagrangian interpolation technique; first derivatives at 688.5, 706.5, 736.5, and 751.5 nm were used in four-point extrapolation method.

Box plots for the REP results of each class from both the field and indoor measurements are shown in Fig. 8. Several basic statistical measures of each set of data are interpreted in those box plots.

The red line inside every box indicates the mean value, the top and bottom lines of the box represent the 75th and 25th percentile, and two ends of whiskers show the minimum and maximum of every dataset. All red crosshairs are considered as outliers since those data have a distance with the nearer quartile of more than 1.5 times of the height of the box.

From those box plots, the dispersion degree of every dataset can be easily interpreted. HEA_PCR_N has highest mean values while S_PCR_P has the lowest, regardless the calculation method and experimental environment. Due to the limited amount of samples and the background introduced, each class from the field measurement has larger variance than that from the indoor measurement. In the indoor measurement result, the mean REPs calculated by both methods shifts to shorter wavelength as leaf infection degree becomes more severe. NS_PCR_N and NS_PCR_P samples have REPs between HEA_PCR_N and S_PCR_P.

2.4. MS and HS image processing

Unlike image classification for different land covers or vegetation, this project of citrus disease detection is targeted on the same vegetation, thus more accurate classification criteria are required. Many supervised classification and spectral mapping methods in ENVI were performed to evaluate their adaptability for citrus HLB detection, such as parallelepiped, minimum distance (MinDist), Mahalanobis distance (MahaDist), spectral angle mapping (SAM), spectral information divergence (SID), mixture tuned matched filtering (MTMF), and spectral feature fitting (SFF). Other methods such as maximum likelihood (MaxLik), support vector machine (SVM), and neural network (NN) were also tried, but did not work well in this case.

2.4.1. HS image dimension reduction

Principle component (PC) and MNF are considered as the most important data transformation methods to keep the most useful information with the least number of bands or dimensions in the HS images.

By exporting every pixel spectrum from those six classes presented in Fig. 6, the principle component analysis (PCA) was conducted using MATLAB (version R2010b, MathWorks, Natick, MA, USA) to extract the most information with a least number of bands. Two and three-dimensional graphs (shown in Fig. 9) for different classes are plotted in PC space. Shadow, sand, and soil can be easily separated from vegetation classes even in 2D PC space (Fig. 9a), grass is also separable from healthy and HLB canopies, especially in 3D PC space (Fig. 9b). But large amount of HLB and healthy
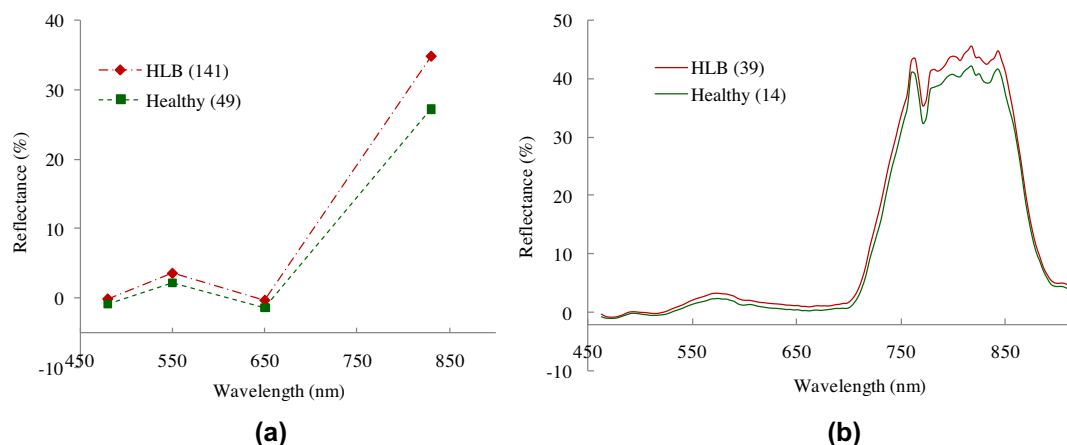

Fig. 7. Mean spectra for healthy and HLB libraries in the 2010 SG images: (a) MS image, and (b) HS image.
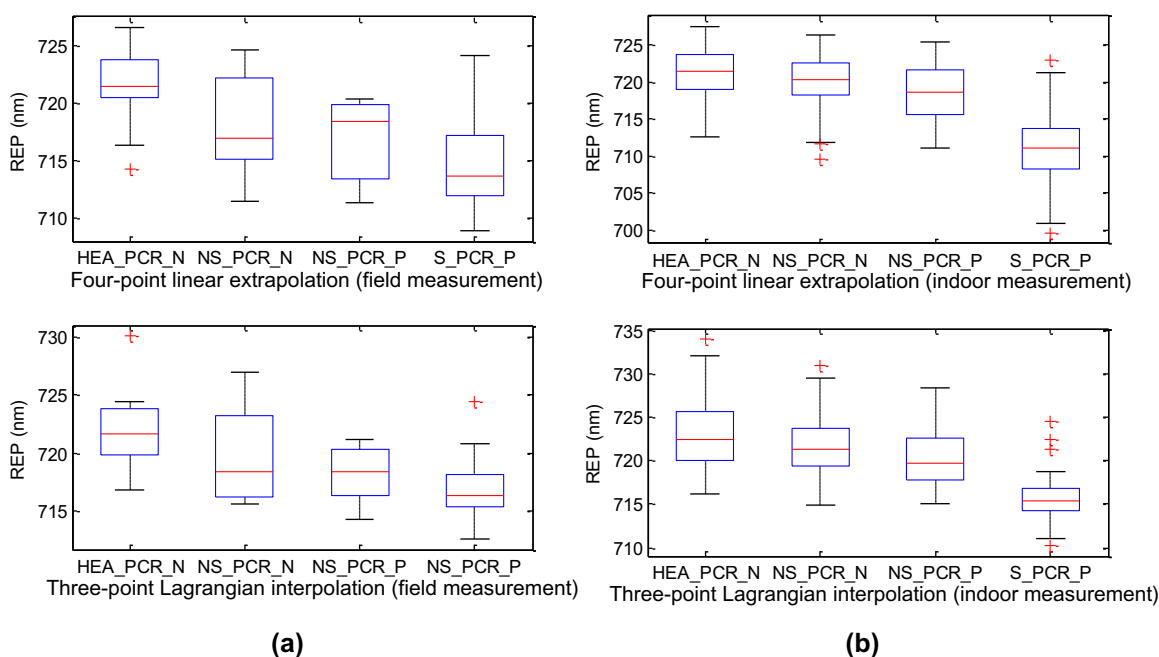
Fig. 8. Boxplots for REP positions of different classes from both the field and indoor measurements: (a) the field measurement, and (b) the indoor measurement.
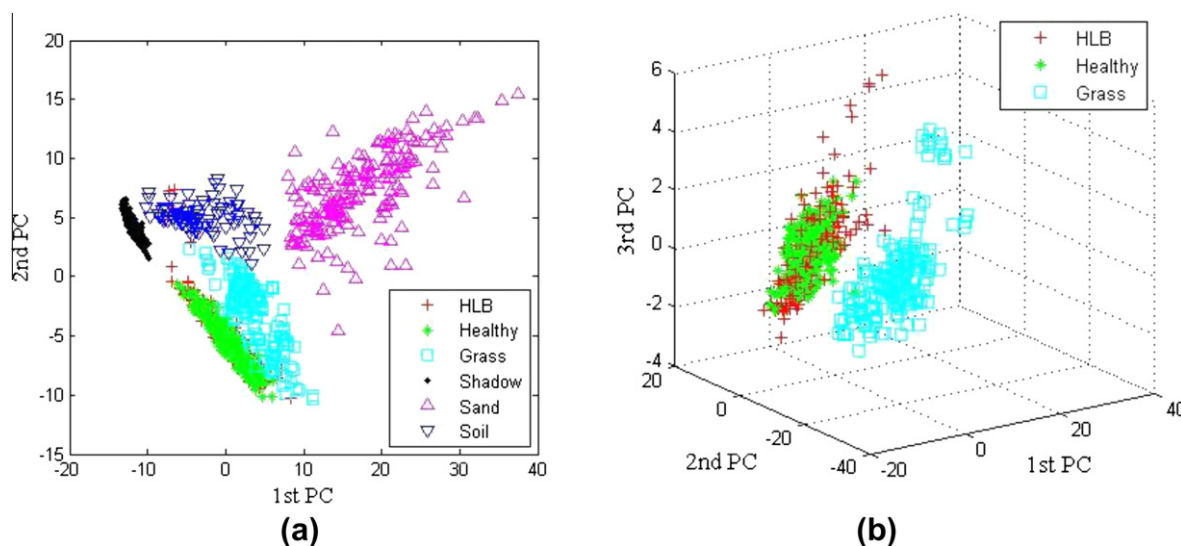

Fig. 9. Scatter plots in PC space (2007 subset image): (a) six classes in 2D PC space, and (b) three vegetation classes in 3D PC space.

pixels are mixed with each other, indicating a tough classification task.

2.4.2. Background masking

In order to avoid influence from grass, shadow, and bare ground, an image mask for tree canopy is necessary to block out the noisy background. Several methods can be used to meet this purpose. Vegetation indices (VIs) are commonly utilized for this purpose by deciding a proper threshold between trees and background; however the reflectance in 2010 images were only calibrated with ground tarps by using an empirical line method, which produced negative values at some pixels with low reflectance (Smith and Milton, 1999; Staben et al., 2011), thus not suitable for VIs calculation. In this case, instead of VIs, SVM was chosen and, in fact, proved to be a more effective alternative to build a mask. SVM forms a decision surface (commonly called an optimal hyperplane) which maximizes the margin between classes to

separate them. Data points closest to the hyperplane are called support vectors which are the critical elements of the training set.

A 100 by 100 pixels HS image (Fig. 10a) with various types of cover was chosen to implement SVM classification. Training ROIs for five classes (tree, grass, shadow, sand, and soil) as defined in Table 3 were collected from the original image. The classification result is shown in Fig. 10b. Since every class in the original image could also be differentiated based on human vision, another result (shown in Fig. 10c) was manually discriminated as a reference to evaluate the classification accuracy.

A confusion matrix was produced to quantify the classification accuracy and is presented in Table 4 with errors of commission and omission. Error of commission occurs when pixels associated with other classes are incorrectly identified as current class; error of omission occurs whenever SVM simply does not recognize pixels that should have been identified as a particular class. The confusion matrix shows that among 3572 canopy pixels in Fig. 10c, 3182 pixels
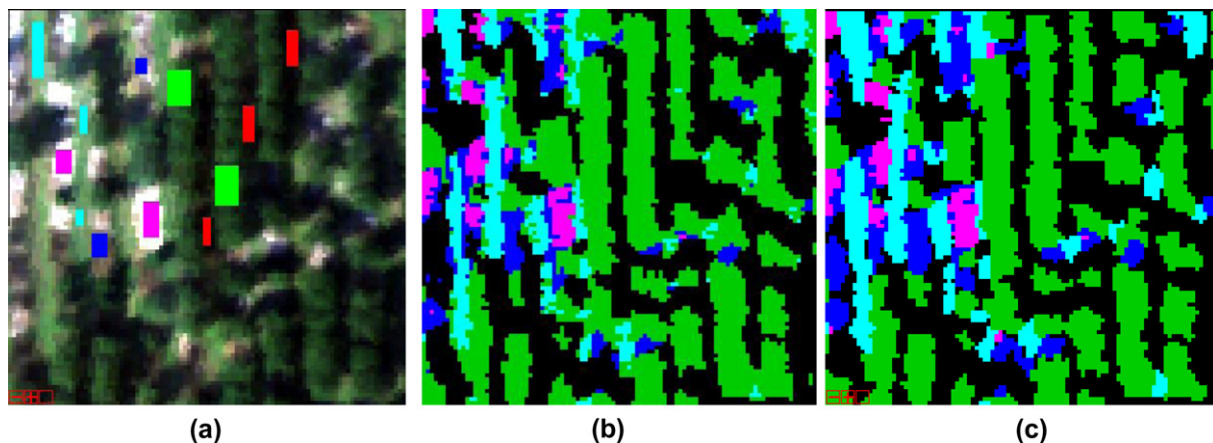
Fig. 10. SVM classification accuracy evaluation (2007 subset image): (a) original subset image, (b) SVM classification result, and (c) manually defined ROIs by human vision.

Table 3
ROI colors in the classification images and their corresponding classes.

ROI color	Class
Green	Tree canopy
Cyan	Grass
Red, black	Shadow
Blue	Soil
Magenta	Sand

Table 4
Confusion matrix for SVM classification result.

Class (pixel)	Tree	Grass	Soil	Sand	Shadow	Commission (%)
SVM_Tree	3182	242	91	6	369	18.2
SVM_Grass	75	781	19	2	23	13.2
SVM_Soil	1	62	484	42	41	23.2
SVM_Sand	0	0	15	245	0	5.8
SVM_Shadow	314	89	288	8	3631	16.1
Total	3572	1174	897	303	4064	
Omission (%)	10.9	33.5	46.0	19.1	10.7	

were classified correctly as tree canopy; 314, 75, and 1 pixels were incorrectly classified as shadow, grass, and soil, respectively. The error of omission for tree class was 10.9%. However, most of misclassification happened between tree and shadow, which is obviously caused by the unclear boundary between those two classes. Since this study was only concentrated on the bright canopy area, this ambiguous area actually did not affect much on the final result. By ignoring this uncertain area, a modified error of omission and commission for tree class can be re-calculated by Eq. (1) and (2), which were highly improved. The classification result for tree canopy was then used to build a mask for further HLB detection.

$$\text{Modified error of omission for tree class}: \quad \frac{75+1}{3572} * 100\%$$
$$= 2.1\% \tag{1}$$

$$\text{Modified error of commission for tree class}: \quad \frac{242+91+6}{3890}$$
$$* 100\% = 8.7\% \tag{2}$$

2.4.3. Image classification

The 2010 CREC images were not chosen for classification analysis due to an obvious uncorrectable distortion observed in the HS image. In the 2007 HS image, five 100 by 100 pixels subset images were randomly chosen to implement classification methods. Two of them were used as a training set, and the remaining three formed a validation set. Eighty-two and 94 HLB infected trees were found in the training and validation sets, respectively; the rest of the trees were considered healthy. HLB and healthy pixels from the training set were collected as libraries. In the 2010 SG images, most of the ground truth was concentrated in a small area shown in Fig. 11a. This area had 200 by 200 pixels in MS image and 100 by 100 pixels in HS image. The right half area (200 by 100 for MS image, 100 by 50 for HS image) was used as a training set, and the left half as a validation set. Pixels from S_PCR_P (39 samples) in the training area were collected as an HLB library (marked with red crosshairs in Fig. 11a), and pixels from HEA_PCR_N (14 samples) in the training area (marked with white crosshairs in Fig. 11a) formed a healthy library.

Different classification methods were carried out through both training and validation sets by using the library built from the training area. The classification result which best fit the ground truth in the training set was then used to compare with the ground truth in the validation set to calculate detection accuracy. In the 2010 SG image, both S_PCR_P and NS_PCR_P classes were considered as HLB infected trees (41 in the training area and 42 in the validation area) when calculating the detection accuracy.

A visualized plot of HLB and healthy training pixels in MS band space is shown in Fig. 11b. An overlap can be spotted between HLB pixels (red crosshairs) and healthy pixels (green 'x' marks).

To develop a better algorithm for HLB detection, the following methods were compared and evaluated: parallelepiped, minimum distance (MinDist), Mahalanobis distance (MahaDist), spectral angle mapping (SAM), spectral information divergence (SID), spectral feature fitting (SFF), and mixture tuned matched filtering (MTMF).

Parallelepiped classification forms a simple decision boundary which is an *n*-dimensional box or parallelepiped in image data space to classify data. MinDist actually refers to minimum distance to class means; it is another simple method which only calculates the Euclidean distance between each unknown pixel vector and the mean vector of each class. Compared to MinDist, MahaDist classification not only calculates the Euclidean distance between unknown pixel and the mean, but also has directional sensitivity. It takes into account how noteworthy this distance is by calculating statistical information of each dataset, but yet fast (Richards and Jia, 2006).

SAM is a physical-based spectral classification method that uses an *n*-dimensional angle to match pixels to reference spectra. It was developed by Boardman (Kruse et al., 1993) which determined the similarity between two spectra by calculating the angle and treat-
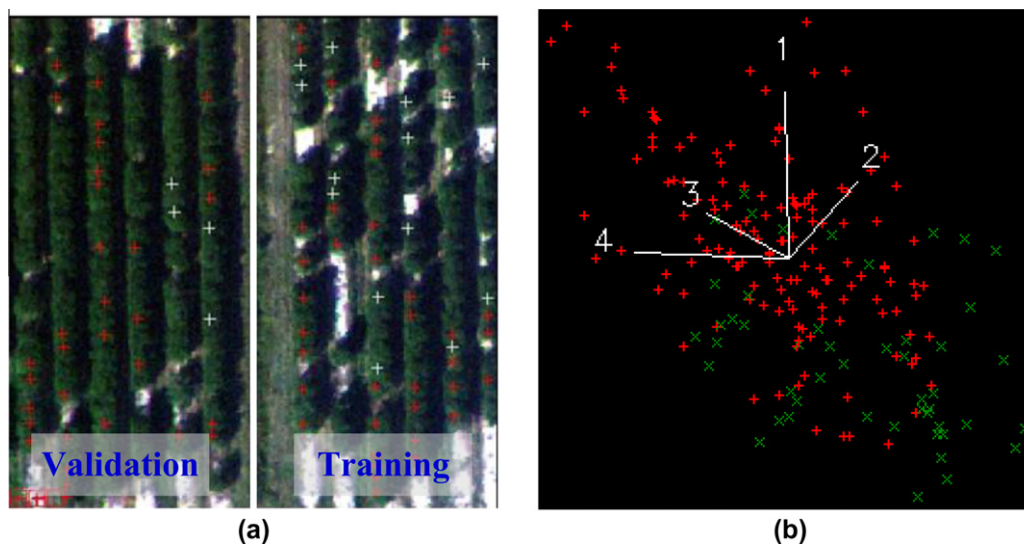
Fig. 11. Subset image for classification and n-D Visualizer for the HLB and healthy libraries (from 2010 SG MS image): (a) true color image of the subset area; red crosshairs infer to HLB infected tree samples, white crosshairs infer to healthy tree samples; the right half for training and left half for validation; (b) n-D Visualizer for HLB (red plus) and healthy (green cross) canopy libraries; Axes 1–4 represent the blue (480 nm), green (550 nm), red (650 nm), and NIR (830 nm) band in the MS image, respectively. (For interpretation of the references to color in this figure legend, the reader is referred to the web version of this article.)

ing them as vectors in a space with dimensionality equals to the number of bands in use (Richards and Jia, 2006). All the four classification methods mentioned above (parallelepiped, MinDist, MahaDist, and SAM) need to input proper threshold parameters.

SID is a stochastic spectral information measuring method. It considers a spectrum as a random variable and measures the divergence between spectra. Smaller divergence indicates higher similarity (Chang, 1999; Du et al., 2004). Qin et al. (2009) found a high accuracy of 96.2% to detect citrus canker from normal peels and other conditions based on the hyperspectral images taken in a laboratory condition.

Continuum removal is a newly developed method which is used to normalize the band depth of spectra so that the depth difference of each class can be more obvious and comparable. It mainly works on spectral absorption range, in other words, the reflectance spectra must have a concave in the range of interest (Kokaly and Clark, 1999). The absorption feature retrieved in this method was found to have a significant correlation with leaf nitrogen content, vegetation coverage, etc. (Huang et al., 2004; Wen et al., 2008). SFF classification method is directly based on this technology. A scale image and root mean square (RMS) image are outputted for each class. Higher scale value and lower RMS error indicate a better match with the library.

MNF transform was performed on all the HS images before implementing MTMF. Every MNF band has an eigenvalue, which rapidly decreases with band number (shown as Fig. 12). The larger the eigenvalue is, the more abundant the information is. The first 20 MNF bands were chosen to carry out MTMF mapping method since they had more significant eigenvalues. MTMF conducts matched filtering (MF) on image and additionally adds an infeasibility image to the results which could be used to reduce the false positives found by MF. Pixels with a high infeasibility are likely to be MF false positives. Parker Williams and Hunt (2002) analyzed the coverage of leafy spurge by using MTMF method, and a high determination coefficient of 0.79 was reached when comparing with the ground truth.

3. Results and discussion

3.1. Ground spectral separation result by REP technologies

To separate HEA_PCR_N and S_PCR_P samples by using ground reflectance spectra (dataset interpreted in Fig. 6), a simple method of REP threshold could reach fairly high accuracy. Table 5 shows the overall separation result. The indoor dataset (about 95%) reached higher accuracy than outdoor dataset (about 90%), because indoor measurement had more ideal environment and larger number of samples. Four-point linear extrapolation technique yielded better performance than three-point Lagrangian interpolation. Fig. 13a shows the REP result by four-point linear extrapolation from the 2010 SG indoor measurement. This result shows that REP technique is a promising classification method, at least for ground measurement.

Same techniques were then applied to the 2010 SG HS image, from where, 52 HEA_PCR_N pixels and 109 S_PCR_P pixels were chosen to calculate their REP by Lagrangian interpolation and linear extrapolation, respectively. But neither of those methods produced good result as shown in Fig. 13b which contains the result calculated by linear extrapolation, and little difference could be found. This is probably caused by the low spatial resolution of
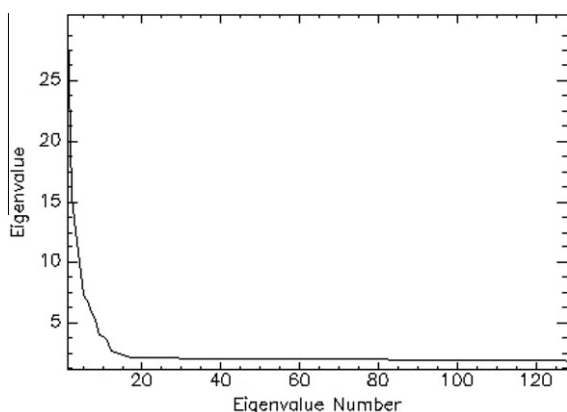

Fig. 12. Eigenvalues for each band after MNF transform (from 2010 SG HS subset image).

Table 5
Separation results between HEA_PCR_N and S_PCR_P classes by using simple REP thresholds, where "LI" means Lagrangian interpolation, "LE" means linear extrapolation.

Experiment	REP method	Threshold (nm)	Accuracy	
			Number of samples	Pct. (%)
2010 SG field measurement (total sample number: 24)	Three-point LI	719.8	21	87.5
	Four-point LE	720.0	22	91.7
2010 SG indoor measurement (total sample number: 136)	Three-point LI	718.2	129	94.5
	Four-point LE	716.5	130	95.6

(a) **(b)**
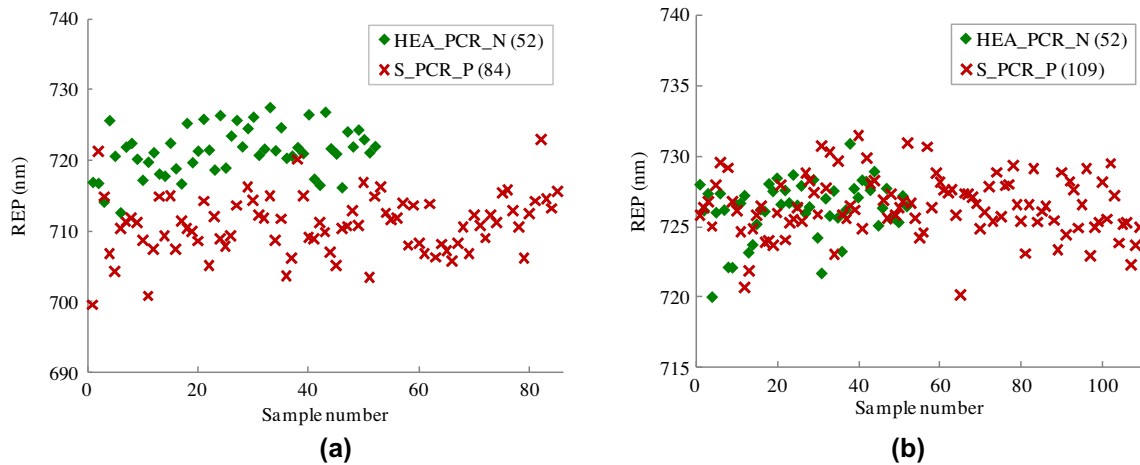
Fig. 13. REP calculation results in the 2010 SG experiment: (a) REP calculated by four-point linear extrapolation from the indoor measurement, (b) REP calculated by four-point linear extrapolation from the HS image.

(a) **(b)**
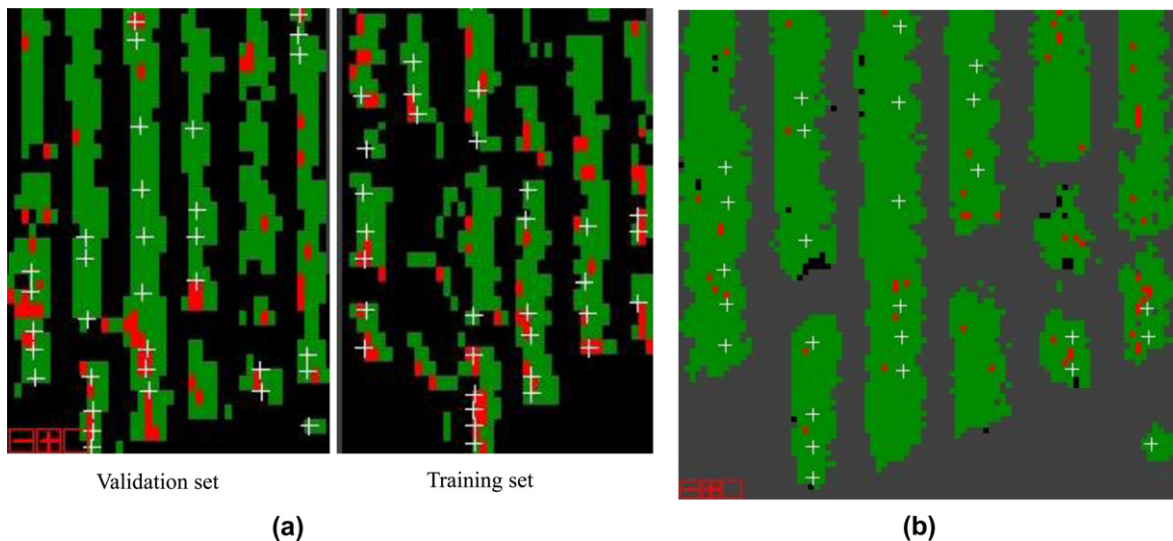
Fig. 14. MinDist and MahaDist classification results: (a) MinDist result from the 2010 HS image, and (b) MahaDist result from the 2010 MS image (validation set).

the image which blurred out the characteristic found in ground measurement.

3.2. Image classification result

Fig. 14a[1] shows part of the result conducted with MinDist method from the 2010 HS image. The green areas indicate healthy tree canopies, and the red rectangles are the HLB detection results. T-he c-

rosshairs show the infected trees which were confirmed by PCR test. Fig. 14b shows part of the classification result by MinDist from the 2010 MS image.

Ground measured reflectance for HLB and healthy canopies were used as libraries in SID and SFF spectral mapping methods. Fig. 15a shows the mean spectral library of HLB and healthy classes from the ground truth. The classification result by SID from the 2010 HS subset image is shown in Fig. 15b.

Fig. 16 shows the classification result by SFF method. A scatter plot is presented in Fig. 16a, in which, x-axis represents the values from the scale image and y-axis represents the values from the
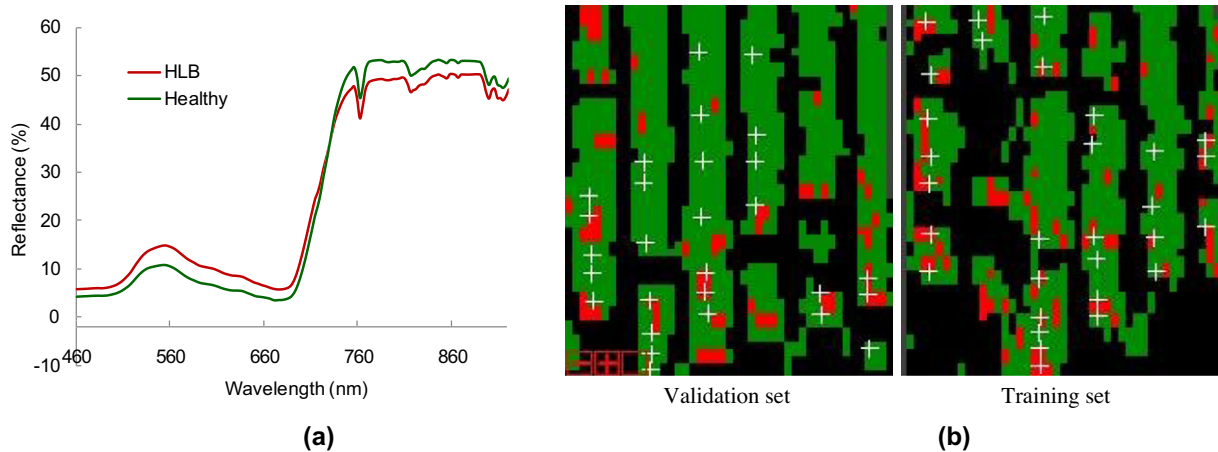
---

[1] For interpretation of color in Figs. 3, 8, 14, 16, and 18, the reader is referred to the web version of this article.

Fig. 15. SID classification result from the 2010 HS image: (a) imported library from the ground measured reflectance, and (b) SID classification result.
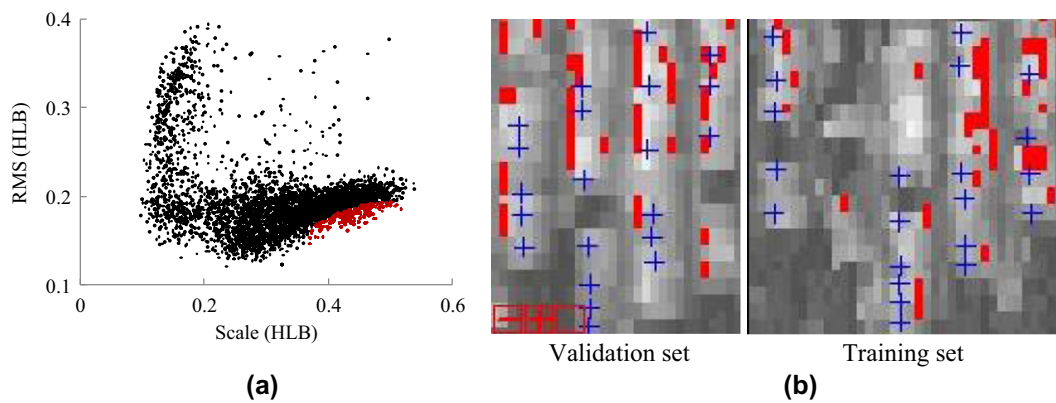

Fig. 16. SFF classification result from the 2010 HS image: (a) SFF scatter plot, and (b) SFF classification result.

RMS image. Higher scale and lower RMS value indicates a better match to the library. The lower right corner in Fig. 16a was selected as infected pixels which are also marked out (red rectangles) in Fig. 16b.

As shown in Fig. 17, a similar scatter plot was generated when MTMF was implemented. x-axis is the MF score, and y-axis is the infeasibility. Every pixel was plotted in the scatter plot according to their MF scores and infeasibility values which were calculated by MTMF mapping method. Pixels which had high MF scores and low infeasibility values (mapping in the lower-right corner in the

scatter plot) were selected out as the infected pixels. Fig. 17b shows the corresponding pixels marked in Fig. 17a.

3.3. Classification result comparison

Since all the ground truth coordinates could only reach tree-level positioning accuracy, average values of neighboring pixels were adopted to build the HLB and healthy libraries, therefore, only tree-based accuracy rather than pixel-based accuracy could be calculated in the classification results. Even though the whole SG grove
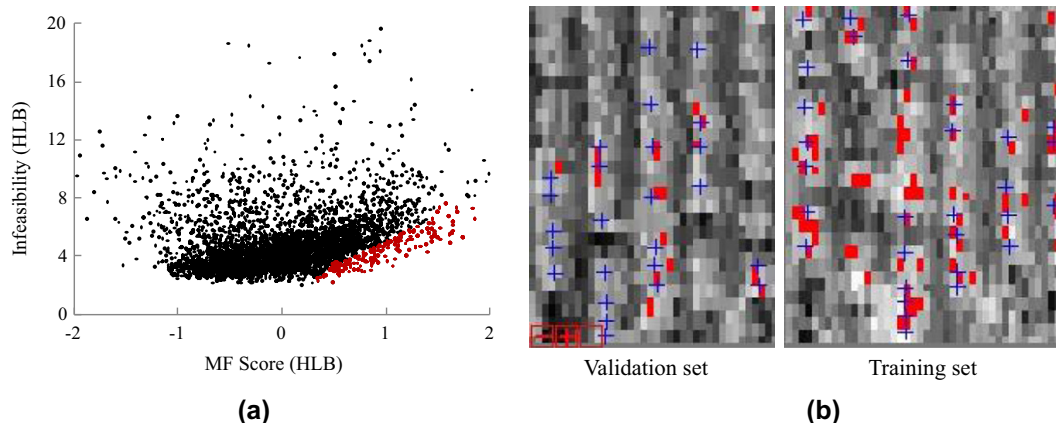

Fig. 17. MTMF mapping result from the 2010 HS image: (a) MTMF scatter plot, and (b) MTMF classification result.

were roughly scouted, and infected trees were recorded by growers, but no PCR tests were conducted to ensure their infection status. Also the positioning errors were too notable to ignore. So it was difficult to count the overall detection accuracy, and only detection accuracy about the PCR confirmed trees could be calculated. Table 6 includes all the tree-based classification accuracy

Table 6
Classification results of different detection methods implemented. Tree based accuracies were calculated for the training (T) and validation (V) sets. Total numbers of PCR confirmed infected tree were included in the parentheses in the "Image" column.

| Image	Method	Correctly identified			
		Training set (T)		Validation set (V)	
		No. of trees	Pct. (%)	No. of trees	Pct. (%)
2007 SG HS image	Parallelepiped	44	53.7	27	28.7
(number of HLB	MinDist	37	45.1	39	41.5
infected trees: T, 82;	MahaDist	82	100	30	31.9
V, 94)	SAM	50	61.0	43	45.7
	SID	33	40.2	28	29.8
	MTMF	62	75.6	50	53.2
	SFF	49	59.8	32	34.0
2010 SG HS image	Parallelepiped	30	73.2	18	42.9
(number of HLB	MinDist	34	82.9	27	64.3
infected trees: T, 41;	MahaDist	31	75.6	32	76.2
V, 42)	SAM	40	97.6	23	54.8
	SID	37	90.2	25	59.5
	MTMF	38	92.7	24	57.1
	SFF	39	95.1	37	90.2
2010 SG MS image	Parallelepiped	39	95.1	25	59.5
(number of HLB	MinDist	37	90.2	28	66.7
infected trees: T, 41;	MahaDist	38	92.7	26	61.9
V, 42)	SAM	39	95.1	26	61.9
	SID	31	75.6	40	95.2
	MTMF	35	85.4	26	61.9

for both training and validation sets in the images taken at the SG grove.

The classification results for the 2007 HS image are not good. The highest correct identification rates are 75.6% for the training set, and 53.2% for the validation set. The main reasons for these low accuracies are: (a) HLB and healthy libraries built from the ground truth in the 2007 experiment were not accurate due to the high positioning error; (b) the 2007 HS image had five subset images from different areas, radiometric differences between each subset (may be caused by the geographic changes, atmospheric particulate variation, etc.) also had negative influence on the classification results.

The 2010 images yielded much better results than the 2007 image. SFF showed very good accuracy of 95.1% in the training set and 90.2% in the validation set in the 2010 HS image, but it did not work well in the MS image, implying that SFF was not a good idea for this four-band MS image. More (but not too many) bands would be needed for a better result. SID yielded abnormal result in the 2010 MS image (detection accuracy in the validation set was much higher than that in the training set), which indicated unstable performance in this application. SAM performed very well in the training set, but its accuracy decreased significantly in the validation set. Simpler classification methods like MinDist and MahaDist showed more stable performance in the 2010 images, as they had more balanced accuracies between the training and the validation sets.

In order to better evaluate each classification method, infection density maps were also generated in ArcGIS (version 9.0, Esri, Redlands, CA, USA) from the ground scouting result (Fig. 18a) and classification results by different algorithms (Fig. 18b–f) in the 2010 HS image. Four degrees of infection were defined according to the infection density: low, medium, high, and severe.

From the density distribution maps, an important phenomenon was noticed: the infection areas and severity produced by classification results are smaller and less than the map generated from the ground scouting result. It meant all the classification methods underestimated the infection severity. The reason was that the
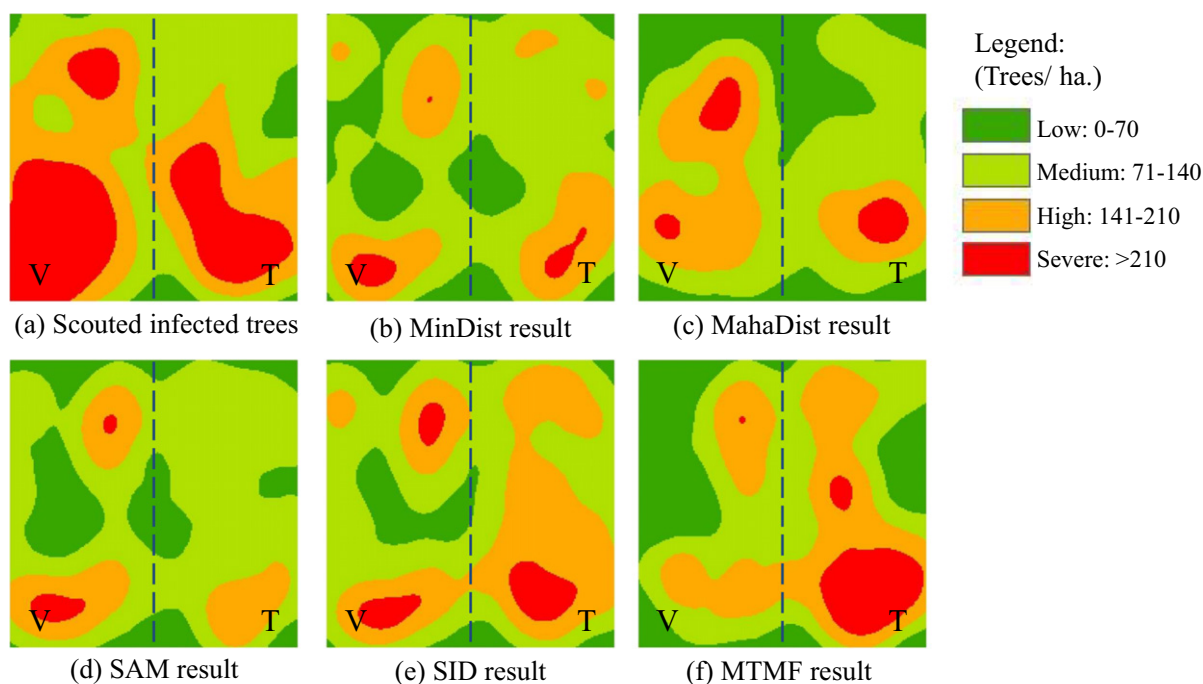
Fig. 18. Density distribution maps, in which the black dashed lines indicate the boundary of the training (T) and validation (V) sets: (a) density map generated from ground scouting by grower; (b–f) density maps generated by different classification results in the 2010 HS image.

classification thresholds were only determined to maximally match the PCR confirmed ground truth which was not fully investigated for all the trees. This problem can be solved by investigating ground truth comprehensively in the training area.

Putting aside the difference of infection severity, MahaDist yielded the best match with the trend of the ground scouted truth map. Since MinDist measures the Euclidean distance from library mean, and SAM is essentially the Euclidean distance (Du et al., 2004) when the spectral angle is small (which is exactly the case in this study because this HLB disease detection is actually based on the same kind of canopy), they produced very similar results with each other. SID and MTMF relatively overestimated the infection situation in the training set and underestimated it in the validation set, indicating an over-fitting problem. But no matter which method was used, the most severely infected areas (red areas in Fig. 18a) were all pointed out, showing a great potential to support citrus grove management. This also indicated that the more severe the disease is, the easier it can be identified. In one word, airborne image could be used to assist citrus grove management since it was capable of detecting the HLB disease with obvious symptom and infection area. Fast and semi-automatic detection procedure could be developed as long as the ground truth in the training area could be investigated as the input. Thresholds in the classification methods could be manually decided. More comprehensive and precise ground truth investigation would produce higher accuracy.

From both the quantified accuracy results and the density maps, the relatively simpler methods – MinDist and MahaDist showed more stable and balanced performance than the rest, thus they were highly recommended in a future study.

Some problems were encountered during this research, especially in the field experiments. To get better results, the following improvements or suggestions needed to be taken into consideration:

(1) Low classification accuracy and high false positive were highly related with large positioning error of the ground truth. More precise ground truthing must be conducted. For example, specific infected canopy locations and areas other than the center coordinates of infected trees should be recorded to exactly pinpoint the research targets. Reliable imaging system was another critical concern to ensure high quality images.

(2) Except MTMF, all other classification or spectral mapping methods were carried out in the original band space, however other data spaces such as MNF space, PC space, etc. should be further considered for better classification results.

4. Conclusions

The MS and HS airborne images of citrus groves were acquired to detect HLB infected trees. Ground truthing including ground reflectance measurement, tree infection status confirmation, and GPS coordinates recording was implemented to analyze the spectral features and build proper libraries for HLB infected and healthy canopies. The following are major findings:

(1) Spectral reflectance was analyzed. Ideally, the healthy canopy had higher reflectance in the visible range, and lower in the NIR range than the infected canopy. But the relationship in the NIR range was easily affected by measuring condition or environment.

(2) REP was comparably less sensitive to the environment than the reflectance in the NIR range. Separation accuracy of more than 90% was reached when simple threshold method was

implemented within ground spectral datasets, regardless of field or indoor measurement; but still did not work well with HS images due to its low spatial resolution.

(3) SVM provided a fast, easy and adoptable way to build mask for tree canopy to block out background pixels for further imaging classification.

(4) Several classification and spectral mapping methods were conducted to evaluate their applicability for HLB detection. High positioning error of the ground truth in the 2007 HS image led the validation accuracy to less than 50% for most of the classification methods. However, with better ground truthing data, the 2010 SG images reached higher accuracies ranging from 43% to 95%. Simpler classification methods, MinDist and MahaDist, showed more stable and balanced performance between the training and validation sets, thus those two methods were highly recommended in a future study.

(5) Most of the methods were able to detect the severely infected areas in the density maps, and their similar infection trend with that of scouted map could provide a promising way to assist HLB disease management. Using the ground truthing in the training area as the prior knowledge, procedures could be developed for rapid detection of the HLB disease.

References

Bajwa, S.G., Bajcsy, P., Groves, P., Tian, L.F., 2004. Hyperspectral image data mining for band selection in agricultural applications. Transactions of the ASAE 47 (3), 895–907.

Boardman, J.W., Kruse, F.A., 1994. Automated spectral analysis: a geologic example using AVIRIS data, north Grapevine Mountains, Nevada. Proceedings of the Thematic Conference on Geologic Remote Sensing 10 (1), 407–418.

Boochs, F., Kupfer, G., Dockter, K., Kühbauch, W., 1990. Shape of the red edge as vitality indicator for plants. International Journal of Remote Sensing 11 (10), 1741–1753.

Candade, N., Dixon, B., 2004. Multispectral classification of Landsat images: a comparison of support vector machine and neural network classifiers. In: ASPRS Annual Conference Proceedings. Denver, Colorado.

Chang, C.I., 1999. Spectral information divergence for hyperspectral image analysis. Geoscience and Remote Sensing Symposium 1, 509–511.

Cho, M.A., Skidmore, A.K., 2006. A new technique for extracting the red edge position from hyperspectral data: the linear extrapolation method. Remote Sensing of Environment 101 (2), 181–193.

Dawson, T.P., Curran, P.J., 1998. A new technique for interpolating the reflectance red edge position. International Journal of Remote Sensing 19 (11), 2133–2139.

DPI, 2010. Section positive for Huanglongbing in Florida, HLB Bibliographical database, FDACS. Available from: <www.crec.ifas.ufl.edu/>.

Du, Y., Chang, C.I., Ren, H., Chang, C.C., Jensen, J.O., D'Amico, F.M., 2004. New hyperspectral discrimination measure for spectral characterization. Optical Engineering 43 (8), 1777–1786.

Gonzalez-Mora, J., Vallespi, C., Dima, C.S., Ehsani, R., 2010. HLB detection using hyperspectral radiometry. In: 10th ICPA Proceedings. Available from: <http://www.andrew.cmu.edu/user/jlibby/robotany/Gonzalez-Mora-2010.pdf/>.

Green, A.A., Berman, M., Switzer, P., Craig, M.D., 1988. A transformation for ordering multispectral data in terms of image quality with implications for noise removal. IEEE Transactions on Geoscience and Remote Sensing 26 (1), 65–74.

Hajj, M.E., Begue, A., Guillaume, S., Martine, J.F., 2009. Integrating SPOT-5 time series, crop growth modeling and expert knowledge for monitoring agricultural practices – the case of sugarcane harvest on Reunion Island. Remote Sensing of Environment 113 (10), 2052–2061.

Halbert, S.E., Manjunath, K.L., 2004. Asian citrus psyllids (Sternorrhyncha, Psyllidae) and greening disease of citrus: a literature review and assessment of risk in Florida. Florida Entomologist 87 (3), 330–353.

Hawkins, S.A., Park, B., Poole, G.H., Gottwald, T., Windham, W.R., Lawrence, K.C., 2010. Detection of citrus huanglongbing by Fourier transform infrared–attenuated total reflection spectroscopy. Applied Spectroscopy 64 (1), 100–103.

Horler, D.N.H., Dockray, M., Barber, J., 1983. The red edge of plant leaf reflectance. International Journal of Remote Sensing 4, 273–288.

Huang, W., Lamb, D.W., Niu, Z., Zhang, Y., Liu, L., Wang, J., 2007. Identification of yellow rust in wheat using in-situ spectral reflectance measurements and airborne hyperspectral imaging. Precision Agriculture 8 (4–5), 187–197.

Huang, Z., Turner, B.J., Dury, S.J., Wallis, I.R., Foley, W.J., 2004. Estimating foliage nitrogen concentration from HYMAP data using continuum removal analysis. Remote Sensing of Environment 93, 18–29.

Jagoueix, S., Bove J.M., Garnier, M., 1996. Techniques for the specific detection of the two Huanglongbing (greening) liberobacter species, DNA/DNA hybridization and DNA amplification by PCR. In: 13th IOCV Conference.

Johnson, L.F., Roczen, D.E., Youkhana, S.K., Nemani, R.R., Bosch, D.F., 2003. Mapping vineyard leaf area with multispectral satellite imagery. Computers and Electronics in Agriculture 38 (1), 33–44.

Knipling, E.B., 1970. Physical and physiological basis for the reflectance of visible and near-infrared radiation from vegetation. Remote Sensing of Environment 1 (3), 155–159.

Kokaly, R.F., Clark, R.N., 1999. Spectroscopic determination of leaf biochemistry using band-depth analysis of absorption features and stepwise multiple linear regression. Remote Sensing of Environment 67, 267–287.

Kruse, F.A., Lefkoff, A.B., Boardman, J.W., Heidebrecht, K.B., Shapiro, A.T., Barloon, P.J., Goetz, A.F.H., 1993. The spectral image processing system (SIPS) – interactive visualization and analysis of imaging spectrometer data. Remote Sensing of Environment 44 (2–3), 145–163.

Kumar, A., Lee, W.S., Ehsani, R., Albrigo, L.G., Yang, C., Mangan, R.L., 2010. Citrus greening disease detection using airborne multispectral and hyperspectral imaging. In: International Conference on Precision Agriculture.

Manjunath, K.L., Halbert, S.E., Ramadugu, C., Webb, S., Lee, R.F., 2008. Detection of 'Candidatus Liberibacter asiaticus' in *Diaphorina citri* and its importance in the management of citrus Huanglongbing in Florida. Phytopathology 98 (4), 387–396.

Parker Williams, A., Hunt, E.R., 2002. Estimation of leafy spurge cover from hyperspectral imagery using mixture tuned matched filtering. Remote Sensing of Environment 82 (2002), 446–456.

Plaza, A., Benediktsson, J.A., Boardman, J.W., Brazile, J., Bruzzone, L., Camps-Valls, G., Chanussot, J., Fauvel, M., Gamba, P., Gualtieri, A., Marconcini, M., Tilton, J.C., Trianni, G., 2009. Recent advances in techniques for hyperspectral image processing. Remote Sensing of Environment 113 (S1), 110–122.

Pydipati, R., 2004. Evaluation of classifiers for automatic disease detection in citrus leaves using machine vision. MS thesis. University of Florida, Gainesville, FL.

Qin, J., Burks, T.F., Ritenour, M.A., Bonn, W.G., 2009. Detection of citrus canker using hyperspectral reflectance imaging with spectral information divergence. Journal of Food Engineering 93 (2), 183–191.

Qin, Z., Zhang, M., 2005. Detection of rice sheath blight for in-season disease management using multispectral remote sensing. International Journal of Applied Earth Observation and Geoinformation 7, 115–128.

Richards, J.A., Jia, X., 2006. Remote Sensing Digital Image Analysis: An Introduction. Birkhäuser.

Shafri, H.Z.M., Hamdan, N., 2009. Hyperspectral imagery for mapping disease infection in oil palm plantation using vegetation indices and red edge techniques. American Journal of Applied Sciences 6 (6), 1031–1035.

Shafri, H.Z.M., Suhaili, A., Mansor, S., 2007. The performance of maximum likelihood, spectral angle mapper, neural network and decision tree classifiers in hyperspectral image analysis. Journal of Computer Science 3 (6), 419–423.

Smith, G.M., Milton, E.J., 1999. The use of the empirical line method to calibrate remotely sensed data to reflectance. International Journal of Remote Sensing 20 (13), 2653–2662.

Smith, K.L., Steven, M.D., Colls, J.J., 2004. Use of hyperspectral derivative ratios in the red-edge region to identify plant stress responses to gas leaks. Remote Sensing of Environment 92 (2), 207–217.

Staben, G.W., Pfitzner, K., Bartolo, R., Lucieer, A., 2011. Calibration of WorldView-2 satellite imagery to reflectance data using an empirical line method. In: 34th International Symposium on Remote Sensing of Environment. Sydney, Australia.

Tian, Y.C., Yao, X., Yang, J., Cao, W.X., Hannaway, D.B., Zhu, Y., 2011. Assessing newly developed and published vegetation indices for estimating rice leaf nitrogen concentration with ground- and space-based hyperspectral reflectance. Field Crops Research 120 (2), 299–310.

USDA, 2010. Citrus Fruits 2010 Summary, National Agricultural Statistics Database. USDA National Agricultural Statistics Service, Washington, DC. Available from: <www.nass.usda.gov/>.

Wen, X., Hu, G., Yang, X., 2008. Extraction vegetation coverage from hyperspectral remote sensing image using spectral feature fitting. Geography and Geo-Information Science 24 (1), 27–30.

Yang, C., 2010. An airborne four-camera imaging system for agricultural applications. ASABE Paper No. 1008855, St. Joseph, Michigan.

Yang, C., Everitt, J.H., Davis, M.R., Mao, C., 2003. A CCD camera-based hyperspectral imaging system for stationary and airborne applications. Geocarto International 18 (2), 71–80.